Switching Converter Systems for Fuel Cell Powered Electric Vehicles

Nuno Filipe Lima Guerreiro
nuno.l.guerreiro@tecnico.ulisboa.pt

Instituto Superior Técnico, Lisbon, Portugal

October 2020

ABSTRACT

This dissertation aims to study and develop switching power converters capable of enabling an alternative fuel cell-powered electric vehicle. A particular emphasis on metal-air cells was pursued, namely in the form of aluminium-air fuel cells, as their simple construction, mechanical rechargeability, recyclability, low cost, and high specific energy present interesting advantages, albeit not without challenges. The resulting experimental powertrain is comprised of a high-voltage hybrid parallel configuration of fuel cells and ultracapacitors, as this combination was found to greatly enhance the synergies between both technologies, whilst mitigating their drawbacks. In order to improve performance, efficiency, and reliability, an interleaving topology for the DC/DC Converters was favoured, which alongside the adoption of advantageous SiC-based semiconductors, enabled very high peak efficiencies. Additionally, both the DC/DC Converters and Inverter employed high switching frequencies, in order to further decrease the required filters. The system control strategy is based on the bidirectional power flow ability of the ultracapacitors, and takes advantage of their excellent transient response. Additionally, it features open-circuit semiconductor fault tolerant interleaving, by means of a reconfigurable modulator, and also short-circuit current limiters. The proposed systems were modelled through Matlab/Simulink and their behaviour was successfully validated in normal operation and in fault conditions.

Keywords: Electric Vehicles; Fault Tolerant; Fuel Cells; Interleaving; Switching Converters; Ultracapacitors.

1. Introduction

1.1. Motivation

The ever-increasing harmful effects of greenhouse gas emissions (GHG) have led to strict long-term environmental targets and drastic policy changes [1]. For instance, some European countries have outright banned the future purchase of new combustion engine-based vehicles, as the transportation sector alone represents 28% of all European GHG emissions, with road transport in turn being responsible for over 70% of these emissions [2].

In this context, the electric vehicle (EV) has received increasing attention and importance due to its far less polluting nature and higher efficiency, when compared to traditional internal combustion engine (ICE) solutions [3]. These factors currently make EVs the primary viable alternative with regard to road transport [4].

However, despite their advantages, traditional battery-based electric vehicles (BEV) still present very low market penetration [4], as the comparatively high initial cost, limited driving range, availability of chargers, and long recharge times, significantly hinder the public's opinion and purchasing decisions [5, 6].

Despite the currently perceived issues of BEVs, other solutions have been introduced to the market, such as fuel cell-based electric vehicles (FCEV). These have been mostly hydrogen-powered, and, owing to the hydrogen fuel-cycle's existing problems, expensive fuel cells, safety concerns, and complex storage/fuelling stations [7], FCEVs present even lower market penetration than BEVs, despite solving some of their perceived issues [8].

Nevertheless, funding and research into other alternative energy storage technologies continues to increase, particularly in China, where severe air pollution and an ever-growing population drive the need for alternative transport solutions [9].

Alongside these developments, power semiconductors continue to evolve, leading to increasing efficiency gains, higher operational frequencies, and better power densities [10].

Hence, some of these alternative energy storage technologies, coupled with the existing advantages and versatility of switching power converters, by means of an optimized architecture and control strategy, may help solve some of the problems that are currently perceived by the public, and thus present potential alternatives for future electric vehicles.

1.2. Objective

The main aim of this thesis is to develop switching power converters and to define their control strategy, in order to enable an alternative fuel cell-powered solution, potentially capable of addressing some of the issues of current electric vehicles.

In order to achieve this objective, it is necessary to accomplish the following intermediate goals:

- Size the chosen energy storage system, switching converters, and electric motors;
- Design the switching converter architecture capable of interfacing the electric motors to the fuel cell-based energy storage system;
- Obtain the dynamic models of the system;
- Design the system's control architecture;
- Simulate the system's comparative performance.

2. Energy Storage Systems

After an in-depth analysis of the existing energy storage technologies, metal-air cells, namely in the form of mechanically rechargeable metal-air fuel cells (MAFC) were identified as an interesting candidate for the primary energy storage system, with very promising demonstrated prototypes [11, 12].

These electrochemical cells are in essence halfway between a battery and a fuel cell, and can be considered a special type of fuel cell [13], as they share the oxygen reduction reaction of other fuel cell types, and can be mechanically recharged [13]. Their energy is derived from a pair of redox reactions, namely the oxidation of the employed metal, and the oxygen's reduction. As one of their electrode's reagents is oxygen, they generally boast very high gravimetric energy densities (figure 1) [14].

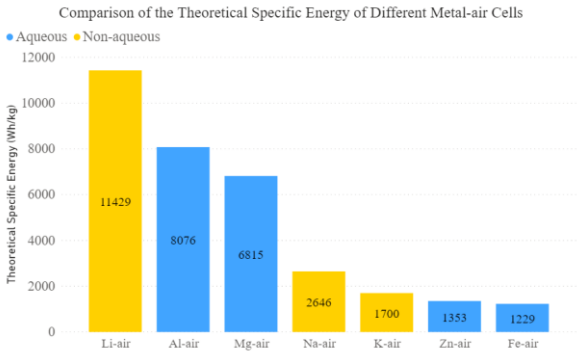

Figure 1: Comparison of the theoretical specific energy of different existing metal-air cells [14].

Due to resource abundance, low cost, recyclability and safety considerations, mechanically rechargeable Aluminium-air (Al-air) fuel cells were selected for the primary energy storage system.

During the operation of Al-air cells, the aluminium anode is consumed, as well as water, resulting in the creation of aluminium hydroxide – a key component of aluminium's existing industrial refining process [15].

$$4\mathrm{Al} + 3O_2 + 6H_2O \rightarrow 4\mathrm{Al(OH)_3}\ (E^0 = +2.75\ V) \quad (1)$$

Historically, these cells have been hindered by the high cost of the employed platinum-based catalysts, similarly to Proton Exchange Membrane fuel cells (PEM), as well as anode self-passivation and parasitic corrosion issues, owing to the reactivity of aluminium and the required alkaline electrolyte [16]. However, progress in the development of aluminium alloys with other trace elements [16], electrolyte additives [16], MnO_2-based catalysts [17], and oleophobic separators [18], continue to improve this technology's potential.

Considering the mobility-oriented application, and aiming for low cost of the catalyst, the selected fuel cell configuration is based on the experimental results obtained by Wang et. al. [19] – through the use of a residual Al-Bi-Pb-Ga alloy and novel MnO_2-based catalyst, in a 4M KOH electrolyte, a gravimetric energy density of 3058 mWh/g was obtained, albeit at a limited discharge current of 100 mA/cm^2.

In order to evaluate the required specifications of the primary energy storage system, the study of a small passenger vehicle's power requirements was carried out, resulting in the projected design specifications of the fuel cell-based energy storage system (table 1).

Table 1: Design Specifications of the Energy Storage Systems

Design Specifications	Fuel Cell System	Ultracapacitor System
Voltage	[325 ; 425] V	[250 ; 450] V
Energy Capacity	330 kWh	225 Wh
Power Output	26 kW	> 120 kW
Weight	308* kg	43 kg

***Includes all necessary structures, reagents and secondary systems [20]**

However, as MAFCs can only provide energy, a secondary bidirectional energy storage system is required. This system shall be responsible for absorbing power injected into the DC bus, as well as helping with the peak loads of the system – resolving the peak power limitations of the primary energy storage system.

Considering the possible existing bidirectional solutions, ultracapacitors were favored, owing to their excellent cycling endurance, fast transient response and static nature. The secondary energy storage system's specifications were also derived from the vehicle's power requirement analysis (table 1).

Hence, the final hybrid energy storage system combines the advantages of the chosen technologies, whilst mitigating their otherwise severe drawbacks.

3. Powertrain

Due to the hybrid nature of the energy storage systems, the vehicle's parallel powertrain (figure 2), although more efficient, becomes more complex. The use of a bidirectional secondary storage system requires an interfacing bidirectional DC/DC converter, which must be capable of boosting the ultracapacitors voltage to a level capable of interfacing the inverter that supplies the motor. However, in reverse operation, when power flows from the motor to the ultracapacitors, care must be taken that the voltage be lowered, in order to not exceed the ultracapacitors' limit.

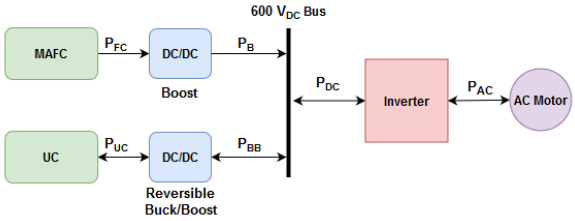

Figure 2: Proposed powertrain configuration.

On the other hand, as MAFCs can only provide energy, their interfacing converter must be unidirectional. However, as this converter interfaces the main energy storage system, it should have maximum efficiency, whilst being compact, as well as, fault tolerant, to enable the vehicle to safely reach its destination in adverse situations.

Additionally, the use of parallel converters allows the fuel cell system to directly power the motor when capable, thus avoiding the compounded losses of a two-stage series DC/DC converter topology. Furthermore, as the combined power output of the energy storage systems can reach 140 kW, a powerful motor can be used, giving the vehicle better driving characteristics.

In order to allow the MAFCs to directly supply the continuous power output required for cruising, the highly efficient AVID's EVO AF130 axial flux motor was chosen [21], which supports a voltage of 600 V_{DC}, thereby enabling lower average currents in the required power converters, which further improves the overall powertrain's efficiency.

4. Power Converters

The topology adopted for the EV drive converter system is based on the system's requirements and relative power flow constraints (figure 3). The MAFC Boost Converter ensures that the unidirectional fuel cell power output is stable, and interfaces it to a common 600 V DC bus. The second converter, which is also connected to the 600 V bus, injects or absorbs current from the bus by use of the ultracapacitor storage system, based on the power flow of the inverter, so as to maintain the DC bus voltage, hence acting as a Reversible Buck/Boost Converter.

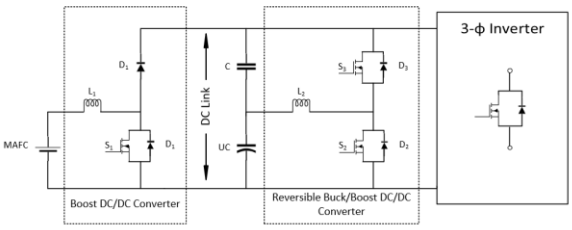

Figure 3: Schematic diagram of EV drive converter system.

Despite the relatively high DC bus voltage, due to the system's peak power output, high currents can still be expected in the converters.

Therefore, in both converters, a three-phase interleaved topology was adopted (figure 4), as this allows a threefold decrease in the semiconductors current ratings and improves the power converters' efficiency, size, electromagnetic emissions and transient response [22, 23]. This design also leads to redundancy in the converters, as, if a converter's phase semiconductors failed, the converter would still operate, albeit at reduced power output [22, 23]. However, this design choice naturally imposes the need for more components.

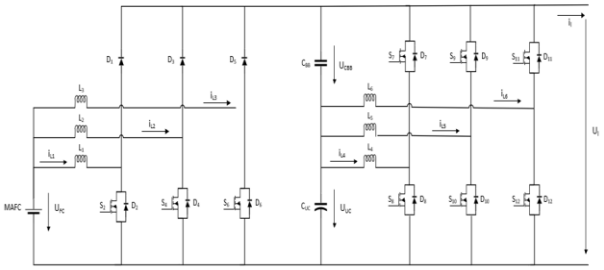

Figure 4: Schematic diagram of the interleaved DC/DC Converters.

The DC/DC Converters were designed according to the typical Boost and Buck/Boost Converter design equations [23].

The duty-cycle can be estimated as [23]:

$$\begin{cases} \delta_{B,min} = 1 - \dfrac{U_{max}}{U_{Bus}} \\ \delta_{B,max} = 1 - \dfrac{U_{min}}{U_{Bus}} \end{cases} \quad (2)$$

In both converters, 10% current ripple was targeted [23]:

$$\Delta i_L = 0.10 \times I_{L\,av,max} \quad (3)$$

As the maximum duty-cycle approaches or surpasses 0.50 for both converters, the inductor's sizing can be made using the critical value equation [23]:

$$L_{crit} = \frac{V_0}{4\Delta i_L} T_{sw} \quad (4)$$

Where $1/T_{sw}$ represents the adopted switching frequency, and V_0 the converter's output voltage.

On the other hand, the filter capacitor required for low voltage ripple can be estimated [23]:

$$C_{BB} = \frac{P_0 \delta_{max}}{V_0 \Delta U_{C_{BB}}} 3T_{sw} \quad (5)$$

In order to allow smaller filter components, as well as to decrease switching and conduction losses, SiC-based semiconductors were favored, thus enabling a switching frequency of 50 kHz.

The peak efficiency of each converter can be estimated by taking into account the losses due to parasitic resistance of the filter components and the MOSFETs conduction and switching losses.

The MOSFETs conduction losses were calculated through their indicated drain-source ON resistance and the root mean square semiconductors' current [23]:

$$P_{C\ MOSFET,B} = R_{DS_{on}} I^2_{SC,RMS} \quad (6)$$

However, their switching losses are comprised of ON/OFF delay losses, and losses associated with the device's output capacitance [23]:

$$P_{sw} = P_{on} + P_{off} + P_{Coss} \quad (7)$$

These, in turn, besides the switching frequency, also depend on the applied drain-source voltage V_{DS}, drain current I_D, turn ON/OFF delay $T_{S\ on/off}$ and the device output capacitance C_{oss} [23]:

$$P_{on,B} = \frac{1}{2} T_{s_{on}} V_{DS} I_D \frac{1}{T_{sw}} \quad (8)$$

$$P_{off,B} = \frac{1}{2} T_{s_{off}} V_{DS} I_D \frac{1}{T_{sw}} \quad (9)$$

$$P_{Coss,B} = \frac{1}{2} C_{oss} V^2_{DS} \frac{1}{T_{sw}} \quad (10)$$

With regard to filter component's losses, they can be estimated by allowing them a percentage loss of the total combined losses, such that the resulting parasitic resistance is feasible to obtain in existing market devices [23]:

$$\frac{P_{rCBB}}{P_0} = \frac{r_{CBB}}{R_{0eq}} \frac{\delta_{max}}{1 - \delta_{max}} \quad (11)$$

$$\frac{P_{rL}}{P_0} = \frac{3 r_L {I_L}^2}{P_0} \quad (12)$$

Due to the relatively low currents experienced by the MAFC Boost Converter and the fact that it interfaces the primary energy source, a high peak efficiency $\eta_B = 99\%$ was targeted.

However, a lower target peak efficiency for the UC Reversible Buck/Boost Converter was unavoidable, as its much higher average currents bound the conduction losses' lower limit, despite the use of similarly advantageous power semiconductors with low ON resistance ratings.

It is important to note that the MAFC Boost Converter's semiconductors were chosen such that each phase individually supports the converter's total power output, thus enabling it to operate unhindered should two phases fail.

Hence, the resulting design specifications of the DC/DC Converters were obtained (table 2).

Table 2: Design Specifications of the DC/DC Converters.

Design Specifications	**MAFC Boost Converter**	**UC Reversible Buck/Boost Converter**
Power Output	$P_{0B} = 25$ kW	$P_{0BB} = 120$ kW
Peak Efficiency	$\eta_B = 99\%$	$\eta_{BB} = 97\%$
Duty-Cycle Range	[0.29 ; 0.46]	[0.25 ; 0.58]
Inductors	1.15 mH	0.40 mH
Filter Capacitor	125 µF	125 µF
Switching Frequency	50 kHz	50 kHz

Similarly, in the design of the Inverter, a high switching frequency was favored in order to entirely avoid the need of burdensome filter inductors, and their respective losses.

The peak torque output of the motor was considered, as, by its torque constant k_T, the worse-case current could be estimated:

$$I_{Phase,RMS} = \frac{T_{max}}{k_T} \quad (13)$$

Similarly to the DC/DC Converters, the Inverter was subsequently designed with an efficiency focus resulting in its projected design specifications (table 3).

Table 3: Design Specifications of the Inverter.

Design Specifications	**Inverter**
Power Output	$P_{0inv} = 150$ kW
Peak Efficiency	$\eta_{inv} = 99\%$
Switching Frequency	70 kHz

Hence, the proposed powertrain is capable of supporting accelerations/braking with a duration of 6 seconds at peak power, allowing for better driving characteristics, and is expected to operate efficiently, particularly during cruising conditions, as the fuel cells may power the motor on their own.

5. Dynamic Models

5.1. UC Reversible Buck/Boost Converter

In order to enable the design of suitable controllers and test the behaviour of the powertrain, dynamic models of its constituents must first be developed.

With regard to the power converters, their topology and design specifications were directly translated into Matlab/Simulink circuit models.

The UC Reversible Buck/Boost Converter consists of an interleaved reversible converter topology capable of operating either in buck or boost mode. In order to achieve this, three identical Reversible Buck/Boost Converters are arranged in parallel, operating with a phase difference of 120° (figure 5).

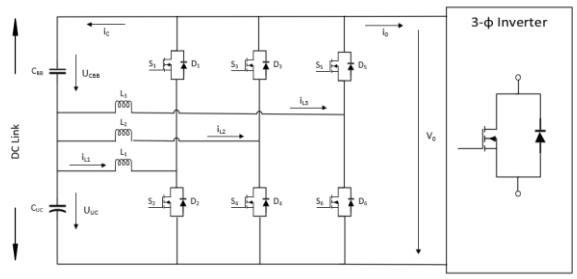

Figure 5: UC Reversible Buck/Boost Converter.

However, despite the converter's interleaved topology, it is possible to fully understand its behaviour by the analysis of one of its constituent phases, as the final converter's behavior is quite similar, besides the phase difference (figures 6 and 7).

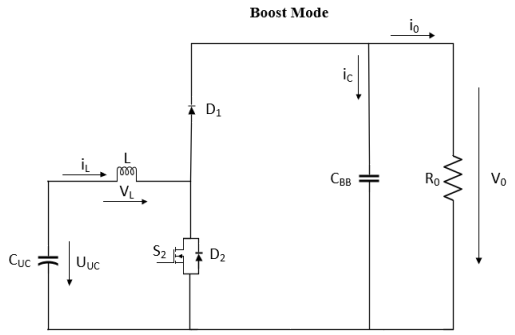

Figure 6: Schematic diagram of the Boost mode.

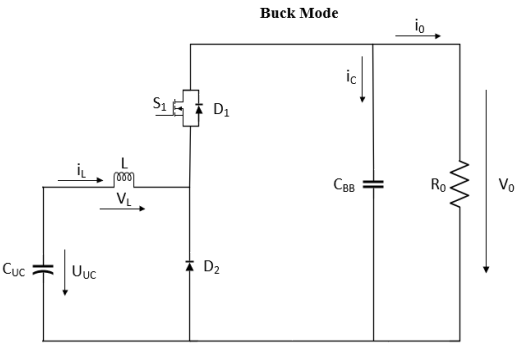

Figure 7: Schematic diagram of the Buck mode.

Due to the complementary behaviour of the transistor's gate signals, it is convenient to define an ON-state variable such that:

$$\Upsilon = \Upsilon_{S2} \Rightarrow \Upsilon_{S1} = \overline{\Upsilon_{S2}} = \bar{\Upsilon} \tag{13}$$

If during $0 < t < \delta T$ the MOSFET S_2 is switched ON ($\Upsilon = 1$) (figure 6), considering a positive inductor current, the current is increased by the ultracapacitors charge. The current through the inductor increases as long as S_2 remains active [23]:

$$0 < t < \delta T \Rightarrow V_L = U_{UC} - r_L i_L \wedge i_L \nearrow \tag{14}$$

During the remainder of the period, $\delta T < t < T$, the MOSFET S_2 is now switched OFF (figure 6) and S_1 is switched ON. Therefore, S_1 will now conduct, transferring energy mainly from the inductor to the output. The current i_L now decreases [23]:

$$\delta T < t < T \Rightarrow V_L = U_{UC} - r_L i_L - V_0 \wedge i_L \searrow \tag{15}$$

It is thus possible to summarize the behaviour of the inductor's time derivative with regard to the transistor's conduction state:

$$V_L = L\frac{\mathrm{di_L}}{\mathrm{dt}} \Rightarrow \frac{\mathrm{di_L}}{\mathrm{dt}} = \frac{U_{UC} - r_L i_L - (1-\Upsilon)\,V_0}{L} \tag{16}$$

As the variation of the inductor's current during a period must be zero:

$$\Delta i_{L_{S2:ON}} + \Delta i_{L_{S2:OFF}} = 0 \tag{17}$$

By neglecting the small voltage drop due to the inductor's parasitic resistance, equations (16) and (17) yield the typical voltage relationship of a Boost Converter, representing this converter's Boost mode [23]:

$$\frac{U_{UC}}{L}\delta T + \frac{U_{UC} - V_0}{L}(1-\delta)T = 0 \Rightarrow V_0 = \frac{U_{UC}}{1-\delta} \tag{18}$$

It is important to note that (18) can be solved for U_{UC} resulting in (19), which means that U_{UC} is smaller than V_0 and the converter will operate in Buck mode if the current $i_L < 0$, transferring power from V_0, by stepping down its voltage, to recharge the ultracapacitors (figure 7) [23]:

$$U_{UC} = (1-\delta)V_0 \tag{19}$$

Hence, a suitable modulator that, not only ensures the necessary phase difference in order for the interleaving topology to work adequately, but that also ensures the complementary behaviour of the MOSFETs in each phase of this converter will be required.

5.2. MAFC Boost Converter

The MAFC Boost Converter's topology is identical to a typical Boost Converter, only it features three of these converters operating in parallel and with a phase difference of 120 degrees (figure 8).

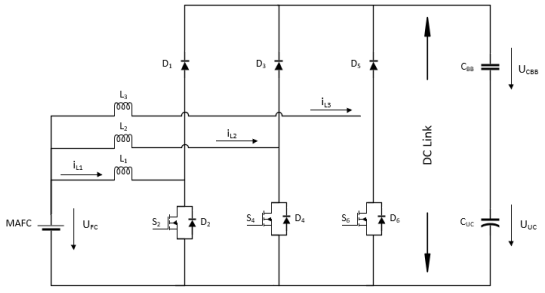

Figure 8: MAFC Boost Converter.

As the MAFC Boost Converter's topology is identical to the Boost mode of the UC Reversible Buck/Boost Converter, all the previous conclusions and equations for its Boost mode apply to this converter.

5.3. Inverter

The required traction Inverter has a typical three-phase two-level topology (figure 9) and will be driven using Space Vector Modulation (SVM). Owing to its phase topological constraints, eight possible switching vectors exist, which govern the phase-to-phase voltages with regard to the DC bus voltage [24].

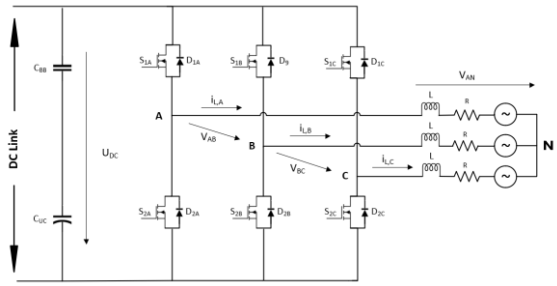

Figure 9: Schematic diagram of the Inverter.

In order to simplify the implementation of SVM, it is useful to employ the Clark-Concordia transformation matrix, which enables the conversion of the three-phase coupled system (ABC 120º reference frame) into a two-phase decoupled orthogonal system ($\alpha\beta$ reference frame). This transformation matrix is given by [23]:

$$\begin{bmatrix} u_\alpha \\ u_\beta \end{bmatrix} = \sqrt{\frac{2}{3}} \begin{bmatrix} 1 & -\frac{1}{2} & -\frac{1}{2} \\ 0 & \frac{\sqrt{3}}{2} & -\frac{\sqrt{3}}{2} \end{bmatrix} \begin{bmatrix} V_{AN} \\ V_{BN} \\ V_{CN} \end{bmatrix} \tag{20}$$

Hence, considering a sweeping command vector, u_{cmd}, which for example lies in the first sector of the SVM voltage space, this vector can be synthetized through the preset voltage-space vectors as [24]:

$$\begin{bmatrix} v^1 & v^2 & v^0 \\ 1 & 1 & 1 \end{bmatrix} \begin{bmatrix} t_1 \\ t_2 \\ t_0 \end{bmatrix} = \begin{bmatrix} u_{cmd} \\ 1 \end{bmatrix} T_s \tag{21}$$

Thus, as the matrix is non-singular, the computation of the duration times can be done in a unique way [24]:

$$\begin{bmatrix} t_1 \\ t_2 \\ t_0 \end{bmatrix} = \boldsymbol{M_1} \begin{bmatrix} u_\alpha \\ u_\beta \\ 1 \end{bmatrix} T_s \Rightarrow \boldsymbol{M_1} = \begin{bmatrix} v^1 & v^2 & v^0 \\ 1 & 1 & 1 \end{bmatrix}^{-1} \tag{22}$$

A symmetric switching sequence is preferred (table 4), as it significantly reduces the output's total harmonic distortion (THD) [24].

Table 4: Symmetric Switching Sequence [24].

Sector	Symmetric Switching Sequence
S_1	$v^0 \rightarrow v^1 \rightarrow v^2 \rightarrow v^7 \rightarrow v^2 \rightarrow v^1 \rightarrow v^0$
S_2	$v^0 \rightarrow v^3 \rightarrow v^2 \rightarrow v^7 \rightarrow v^2 \rightarrow v^3 \rightarrow v^0$
S_3	$v^0 \rightarrow v^3 \rightarrow v^4 \rightarrow v^7 \rightarrow v^4 \rightarrow v^3 \rightarrow v^0$
S_4	$v^0 \rightarrow v^5 \rightarrow v^4 \rightarrow v^7 \rightarrow v^4 \rightarrow v^5 \rightarrow v^0$
S_5	$v^0 \rightarrow v^5 \rightarrow v^6 \rightarrow v^7 \rightarrow v^6 \rightarrow v^5 \rightarrow v^0$
S_6	$v^0 \rightarrow v^1 \rightarrow v^6 \rightarrow v^7 \rightarrow v^6 \rightarrow v^1 \rightarrow v^0$

This Inverter will be commanded through Direct Torque Control (DTC) implemented by means of a typical Variable Frequency Drive (VFD).

5.4. Fuel Cells & Ultracapacitors

A simplified model for the ultracapacitor's and fuel cells was considered. The ultracapacitor's model was derived from their equivalent capacitance and series resistance, assuming that their temperature is well regulated and the charge-state doesn't fall below 30%, as initially projected.

However, the fuel cells simplified model takes into account the experimental polarization curve obtained, from which the activation losses and ohmic losses effects can be estimated [25]:

$$V_{FC} = V_{OC} - V_{L,activation} - V_{L,ohmic} \tag{23}$$

Resulting in the following extended equation which governs the model (figure 10) [25]:

$$V_{FC} = 425 - 50\left(1 - \mathrm{e}^{-0.6 i_{FC}}\right) - 1.25 i_{FC} \tag{24}$$

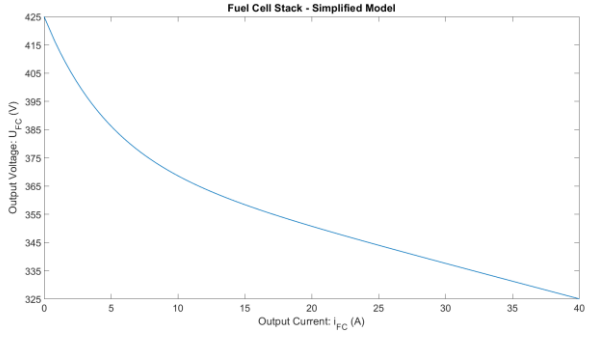

Figure 10: Simplified model of a fuel cell stack.

The final implemented model comprises two parallel fuel cell stacks based on this simplified model.

6. Control Systems

6.1. Modulators

The converter's modulators are of crucial importance as it is their role to ensure the correct phase difference and open-circuit fault tolerance.

In the case of the MAFC Boost Converter, its modulator receives a fault signal from the respective current controller and determines how many phases have failed, adjusting the phase delay to reconfigure the new phase difference (figure 11). The UC Reversible Buck/Boost Converter's modulator is similar, although it instead features the necessary complementary hysteric comparators.

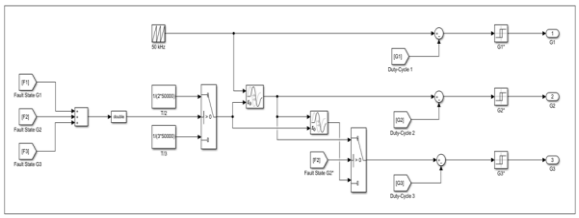

Figure 11: Reconfigurable three-phase modulator.

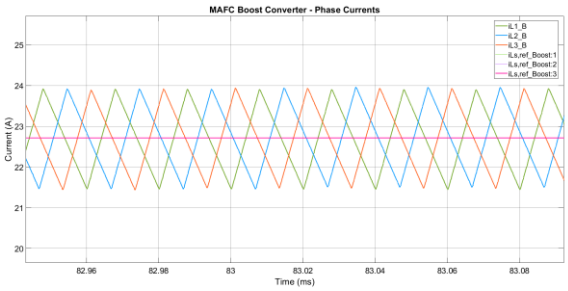

Figure 12: Behaviour of the interleaved phase currents.

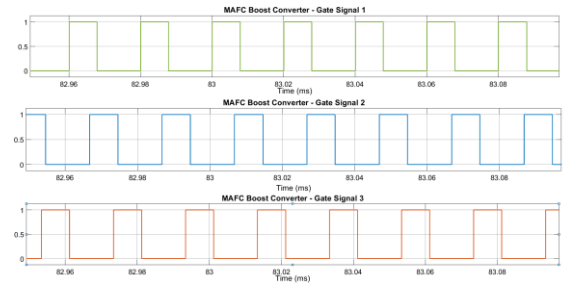

Figure 13: Gate signals of the MAFC Boost Converter.

The reconfiguration of the MAFC Boost Converter's phases in the advent of open-circuit faults was successfully validated (figure 14).

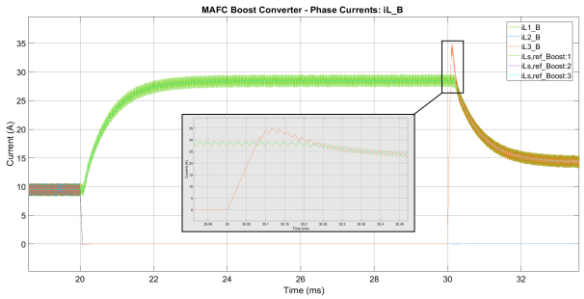

Figure 14: Phase reconfiguration of the MAFC Boost Converter.

6.2. Current Controllers

Despite the phase difference ensured by the modulators, the use of appropriate current controllers is required, otherwise current imbalances would arise.

The system block diagram can be obtained by considering an inductive load/filter and the delay introduced by the modulator, T_D (figure 15).

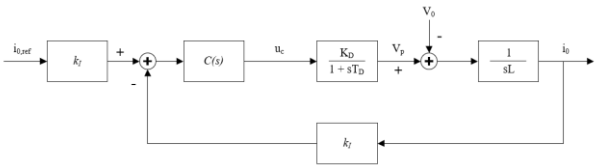

Figure 15: Block diagram of the current controller.

Hence, the following closed-loop transfer function can be derived from the system's block diagram [23]:

$$i_0(s) = \frac{(1+sT_z)i_{0,ref}(s) - sT_p(1+sT_d)V_0(s)}{s^3\frac{LT_pT_d}{K_Dk_I} + s^2\frac{LT_p}{K_Dk_I} + sT_z + 1} \quad (25)$$

In order to ensure minimal steady-state error and fast transient response, a PI Controller per phase was adopted, with dynamics [23]:

$$C(s) = \frac{u_C(s)}{i_{0,ref}(s) - i_0(s)} = \frac{1+sT_z}{sT_p} = K_{pC} + \frac{K_{Tp}}{s} \quad (26)$$

By general application of the *Symmetrical Optimum Criterion*, $b_k^2 = ab_{k-1}b_{k+1}$, the controller's gains can be more finely adjusted [23, 26]:

$$K_{pC} = \frac{T_z}{T_p} = \frac{L}{aT_dK_Dk_I} \quad (27)$$

$$K_{Tp} = \frac{1}{T_p} = \frac{L}{a^3T_d^2K_Dk_I} \quad (28)$$

As factor a enables the fine-tuning of the system's phase-margin and damping factor [23, 26]:

$$\phi_M = \sin^{-1}\left(\frac{a^2-1}{a^2+1}\right) \wedge a = 2\zeta + 1 \quad (29)$$

The MAFC Boost Converter's also features a Supervisor Module (figure 16) capable of identifying open-circuit faults, by comparing the reference current and the phase currents. This information is then fed into the Modulator and a Current Estimator – fully enabling the Converter's reconfiguration in the advent of faults.

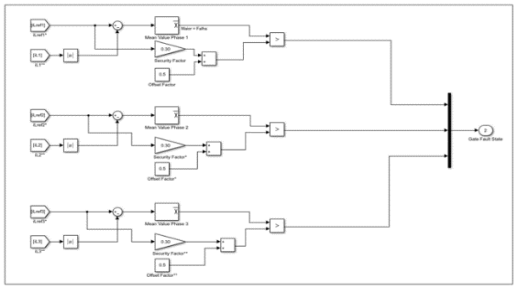

Figure 16: Supervisor Module (open-circuit faults).

6.3. Voltage Controller

To enable adequate voltage control, a cascade control strategy was adopted, which takes advantage of the ultracapacitor's excellent transient response – these devices may quickly inject or absorb current from the DC bus in order to maintain its stability.

Due to these dynamics, the voltage controller is affected by the response delay of the UC Reversible Buck/Boost Converter's current controller (figure 17).

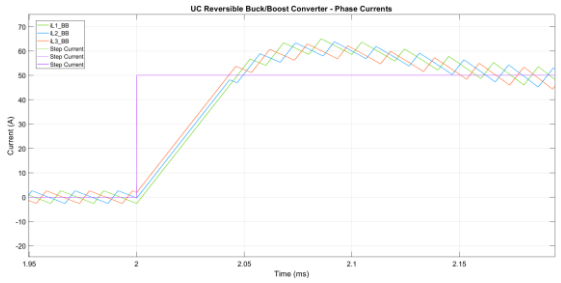

Figure 17: Step response delay of the UC current controller.

Considering the input/output power relationship, the average diode's current can be estimated [23]:

$$P_0 = \eta \mathrm{P}_i \Leftrightarrow i_D V_0 = \eta U_{UC} i_L \Rightarrow i_D = \frac{\eta U_{UC}}{V_0} i_L \qquad (30)$$

On the other hand, the current balance at the filter capacitor's node implies [23]:

$$C_{BB} \frac{dV_0}{dt} = i_D - i_0 = \frac{\eta U_{UC}}{V_0} i_L - i_0 \qquad (31)$$

Hence, equation (31) can be manipulated to allow for the design of a voltage controller based on the square of the output voltage [23]:

$$\frac{C_{BB}}{2} \frac{dV_0{}^2}{dt} = \eta U_{UC} i_L - V_0 i_0 = k_C i_L - V_0 i_0 \qquad (32)$$

The system's block diagram can be thus obtained (figure 18)

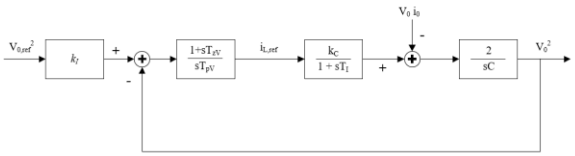

Figure 18: Block diagram of the voltage controller.

A similar application of the *Symmetrical Optimum Criterion* was pursued in order to tune the controller's behavior. Hence the new gain values were used to implement a voltage controller with integral gain-inhibition, to further improve its transient response, as well as short-circuit current limitation (figure 19).

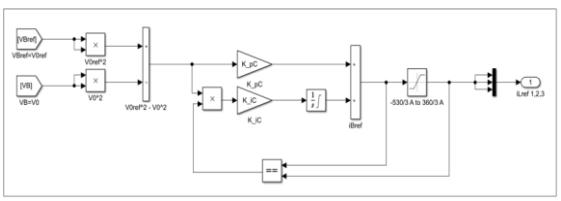

Figure 19: Schematic diagram of the voltage controller [23].

7. System Evaluation

7.1. Scenario

As the driver controls the motor's torque output by means of pedals, owing to the DTC strategy, its variations shall be bound by a lower limit of 100 ms - a worse-case scenario, as this value is significantly smaller than the average driver's reaction time.

Additionally, a sequence of open-circuit phase faults will be considered for the MAFC Boost Converter, in order to evaluate their overall impact on the system's performance and stability (figure 20).

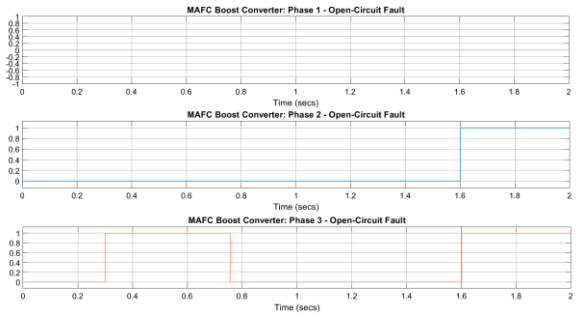

Figure 20: Open-circuit semiconductor fault sequence.

7.2. Results

The system was found to be able to successfully regulate its electromagnetic torque in order to track the reference imposed, with ripple in the order of 3% (figure 21).

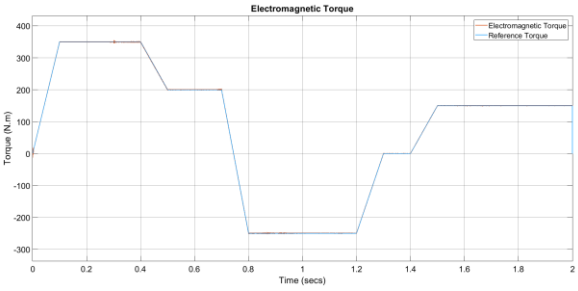

Figure 21: Torque regulation of the motor drive.

The torque profile considered naturally imposed a variation of the rotor's speed (figure 22). This information was used to continuously calculated the expected load torque, considering the vehicle's aerodynamic drag and rolling friction forces.

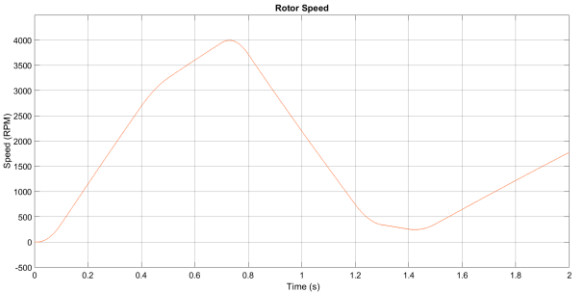

Figure 22: Rotor's speed variation.

The resulting motor drive's behaviour was successfully validated – the stator current's frequency and magnitude increase with the rotor speed and electromagnetic torque, respectively (figure 23).

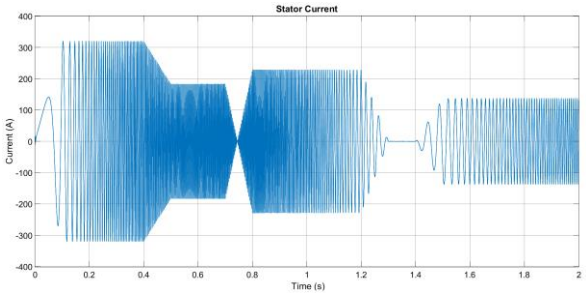

Figure 23: Motor's stator current.

The reference electromagnetic torque profile imposed a well-defined load current profile on the DC bus (figure 24).

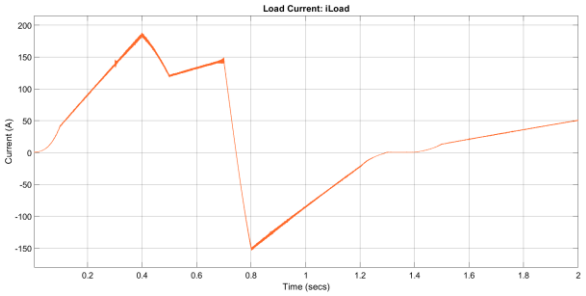

Figure 24: Load current experienced by the DC bus.

As expected, the MAFC Boost Converter delivered up to 25 kW of the experienced load, while the UC Reversible Buck/Boost Converter supplied or absorbed the remaining power (figure 25).

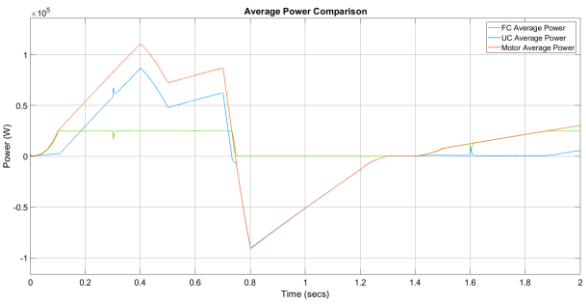

Figure 25: Phase currents of the MAFC Boost Converter.

In the advent of faults, the MAFC Boost Converter successfully reconfigured its phase currents (figure 26).

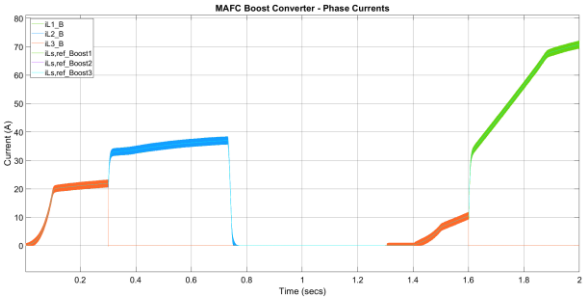

Figure 26: Phase currents of the MAFC Boost Converter.

However, the reconfiguration's impacts on the converter's output current translate into a very brief current loss and the expected aggravation of the output current's ripple – the latter effect is particularly noticeable at t = 1.6 secs, when the converter experiences a double open-circuit fault, thus fully voiding the ripple advantages of an interleaved topology (figure 27).

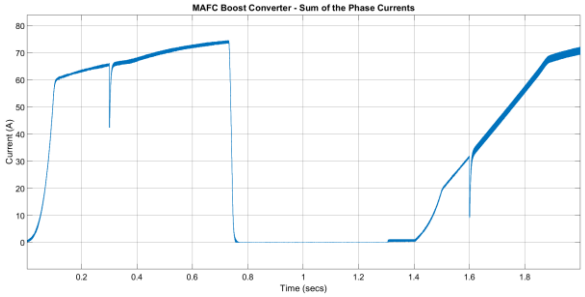

Figure 27: Output current of the MAFC Boost Converter.

The experienced transient current losses, owing to the short delay in the converter's phase reconfiguration, were fully counteracted by the UC Reversible Buck/Boost Converter, resulting in brief current spikes in its output current (figure 28).

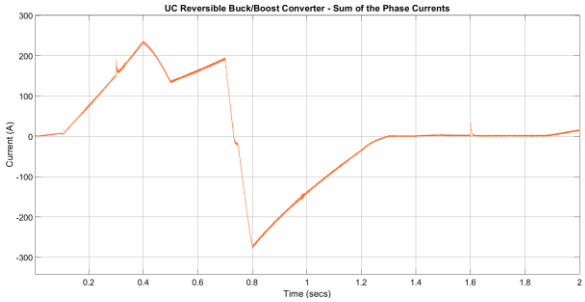

Figure 28: Output current of the UC Buck/Boost Converter.

By the counteracting behavior of the DC/DC Converters, the DC bus voltage is kept within 2% to 3% during normal operation. Nevertheless, in the advent of faults, a total variation of up to the 8% of the system's voltage is experienced, albeit lasting only approximately 2 ms (figure 29)

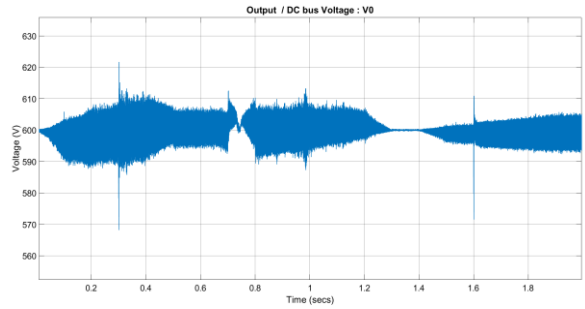

Figure 29: Variations of the DC bus voltage.

Lastly, the resulting voltage variations of the fuel cells and ultracapacitors were also similarly validated, resulting in the expected variations within their specified voltage range, thereby corroborating their developed dynamic models.

8. Conclusions

The versatility of switching converters has enabled an alternative electric vehicle configuration based on Al-air fuel cells and ultracapacitors, which presents very high energy capacity, excellent cycling endurance, enhanced recyclability and minimal safety considerations.

Through the use of a three-phase interleaved topology, the MAFC Boost Converter achieved a peak efficiency of 99%, whilst the UC Reversible Buck/Boost Converter managed to reach 97%. Both Converter's output currents displayed low ripple in the order of 2% to 3%, far lower than the projected 10% for their phase currents, owing to the interleaved topology. Nonetheless, high switching frequencies were employed, as they significantly decreased the ratings of the required filter components. This led to their absence altogether in the case of the Inverter, enabling a peak efficiency of 99%, without compromising heavily on the stator's current total harmonic distortion, which was found to be approximately 0.50%.

Moreover, as the system's control strategy is based on the excellent transient response of the ultracapacitors, fast response times were achieved, aiding the system's overall stability and responsiveness, resulting in the low voltage ripple of the DC Bus. Furthermore, through the reconfigurable modulator developed, the primary energy system is capable of open-circuit semiconductor fault-tolerant operation, without limiting its power output.

The proposed solution poses an interesting alternative, particularly as its power limitations, owing to the fuel cell's low discharge currents, continue to improve.

References

[1] European Commission, A European Strategy for low-emission mobility, Brussels, 2016.

[2] European Environment Agency. "Greenhouse gas emissions from transport in Europe", Copenhagen, 2018.

[3] P. Moura, J. Delgado & A. Almeida. A sustainability assessment of electric vehicles as a personal mobility system, Energy Conversion and Management, Volume 61, 2012, Pages 19-30, ISSN 0196-8904.

[4] International Energy Agency. Global EV Outlook 2019. IEA Publishing: Paris, France, 2019.

[5] W. Li, R. Long, H. Chen H & J. Geng. A review of factors influencing consumer intentions to adopt battery electric vehicles. Renew Sust Energ Rev 78: 318–328, 2017.

[6] Department for Transport. Public attitude towards electric vehicles: 2016. United Kingdom, 2016.

[7] N. Armaroli & V. Balzani. The Hydrogen Issue. ChemSusChem 4, 2011, 216.0.1002/cssc.201000182.

[8] M. A, Hannan, M. Hoque, A. Mohamed & A. Ayob. Review of energy storage systems for electric vehicle applications: Issues and challenges. Renewable and Sustainable Energy Reviews, 69, 2017. 771-789. 10.1016/j.rser.2016.11.171.

[9] F. Zhang & P. Cooke. Hydrogen Fuel Cell Development in China: A Review. European Planning Studies - EUR PLAN STUD. 18. 1153-1168. 10.1080/09654311003791366, 2010.

[10] K. Li, P. Evans & M. Johnson. SiC/GaN Power Semiconductor Devices: A Theoretical Comparison and Experimental Evaluation under Different Switching Conditions. IET Electrical Systems in Transportation, 2017. 10.1049/iet-est.2017.0022.

[11] P. Abrar. Aluminium and air are fuel for this electric vehicle. The Hindu, India, Chennai, November 2018.

[12] V. Jahren. China's Yunnan Aluminium approves battery JV with Israel's Phinergy. Reuters, London, February 2018.

[13] R. P. O'Hayre, S.-W Cha, W.G Collela & F.B. Prinz. Fuel Cell Fundamentals (Third Edition), Section 8.7 - Other Fuel Cells, John Wiley & Sons, Inc., New York, September 2016.

[14] Y. Li & J. Lu. Metal-Air Batteries: Will They Be Future Electrochemical Energy Storage of Choice? ACS Energy Letters, 2, 2017. 10.1021/acsenergylett.7b00119.

[15] M. Pino, J. Chacón, E. Fatás & P. Ocón. Performance of commercial aluminium alloys as anodes in gelled electrolyte aluminium-air batteries, Journal of Power Sources, Volume 299, 2015, Pages 195-201,ISSN 0378-7753.

[16] C. Wang, Y. Yu, J. Niu, Y. Liu, D. Bridges, X. Liu, J. Pooran, Y. Zhang & A. Hu. Recent Progress of Metal–Air Batteries—A Mini Review. Applied Sciences, 9, 2019. 2787. 10.3390/app9142787.

[17] J. Ryu, H. Jang & J. Park. Seed-mediated atomic-scale reconstruction of silver manganate nanoplates for oxygen reduction towards high-energy aluminum-air flow batteries. Nat Commun 9, 3715, 2018, doi:10.1038/s41467-018-06211

[18] B. Hopkins, Y. Shao-Horn & D. Hart. Suppressing corrosion in primary aluminum–air batteries via oil displacement. Science, 362, 2018. 658-661. 10.1126/science.aat9149.

[19] Q. Wang, H. Miao, Y. Xue, S. Sun, S. Li & Z. Liu. Performances of an Al–0.15 Bi–0.15 Pb–0.035 Ga alloy as an anode for Al–air batteries in neutral and alkaline electrolytes. RSC Adv., 7, 2017. 25838-25847. 10.1039/C7RA02918G.

[20] S. Yang & H. Knickle. Design and analysis of aluminum/air battery system for electric vehicles. Journal of Power Sources - J POWER SOURCES. 112, 2002. 162-173. 10.1016/S0378-7753(02)00370-1.

[21] AVID Technology, EVO AF130 Motor (6 turn), 2020. https://avidtp.com/product/evo-motors/

[22] D.J.S. Newlin, R. Ramalakshmi & S. Rajasekaran. A performance comparison of interleaved boost converter and conventional boost converter for renewable energy application. Green High Performance Computing (ICGHPC), 2013, IEEE International Conference. 1-6. 10.1109/ICGHPC.2013.6533924.

[23] J. F. Silva, Electrónica Industrial: Semicondutores e Conversores de Potência. Manuais Universitários, Fundação Calouste Gulbenkian, Lisbon, 2013 Edition, October 2013.

[24] H. Pinheiro, F. Botteron, C. Rech, L. Schuch, R.F. Camargo, H. Hey, H.A. Grundling, & J.R. Pinheiro. Space vector modulation for voltage-source inverters: A unified approach. 1. 23 - 29 vol.1., 2002. 10.1109/IECON.2002.1187476.

[25] A. J. Leon. Modelling and Analysis of Aluminium Air Fuel Cells. Florida Atlantic University, 2013.

[26] C. Bajracharya, M. Molinas, J. Suul & T. Undeland. Understanding of Tuning Techniques of Converter Controllers for VSC-HVDC, 2008.